AIR ENTRAINMENT AND DEGASSING PROCESS IN BREAKING WAVES

A. Iafrati, INSEAN (Italian Ship Model Basin), Rome, Italy,
E-mail: a.iafrati@insean.it

SUMMARY

The air entrainment and the degassing process in breaking waves is investigated. The flow generated by the breaking of free–surface waves of different initial steepnesses is simulated numerically, through a two-fluids Navier-Stokes solver combined with a Level-Set technique for the interface capturing. The flow is assumed two-dimensional. The evolution of periodic wave trains of different initial steepness is considered. For large initial steepnesses the breaking is of the plunging type and leads to the entrappment of large air cavities, area of which is found to scale as the steepness to the power seven. The fragmentation process of the large air cavities is analysed and quantitative estimates of the amount of air entrapped by the breaking and of the degassing process are provided.

1. INTRODUCTION

Breaking of ocean waves is an important mechanism for heat and gas transfer between air and water. The breaking of free–surface waves is characterized by a broad range of scales. Large scale breaking waves are characterized by strong turbulence with a significant amount of drops, spray and bubbles about the breaker front (whitecaps). At the shortest scales, the stabilizing actions of gravity and surface tension dominate over the disrupting effect of the turbulence. The development of the plunging jet is suppressed and only a small amount of air, if any, is entrained (Brocchini and Peregrine, 2001).

In Lamarre and Melville (1991) it was shown that the entrainment of air plays a rather important role on the energy dissipation. Through measurements of the void fraction, they showed that a large portion of the energy dissipated by the breaking, between thirty to fifty per cent, is spent against buoyancy in entrapping air bubbles. After the first plunging event, the large air cavity entrapped is first convected downward and then it is squeezed and fragmented into smaller bubble. The fragmentation process induces a strong vorticity field which rapidly dissipates the potential energy than has been spent in the entrappment and downward convection of the cavity. A similar experimental investigation was recently done by Blenkinsopp and Chaplin (2007). Also in this case it was found that, for strong plunging breaking, at least fourteen per cent of the energy dissipated by the breaking is spent in entraining air and generating splash. The bubble distribution and the fragmentation process of the air cavity entrapped by breaking waves were investigated by Deane and Stokes (2002). They showed that the fragmentation process governs the bubble size distribution up to bubbles larger than 1 mm. Bubbles smaller than that size are stabilized by surface tension forces and do not fragment further.

In this paper the breaking of wave trains with different initial steepness are simulated numerically. The amount of air entrapped by the breaking process is quantitatively evaluated along with the degassing phase. Results are analysed together with the effects of the numerical scheme.

2. NUMERICAL MODEL

The unsteady two-fluids flow of air and water induced by the breaking of free–surface waves is approximated as that of a single incompressible fluid whose density and viscosity vary smoothly across the interface. The problem is governed by the Navier-Stokes equations

$$
\begin{aligned}
\nabla \cdot \boldsymbol{u} &= 0 \\
\frac{D\boldsymbol{u}}{Dt} &= -\frac{1}{\rho}\nabla p + \boldsymbol{f} + \frac{1}{\rho}\nabla \cdot \left[\mu(\nabla \boldsymbol{u} + \nabla \boldsymbol{u}^T)\right] \qquad (1) \\
&\quad + \sigma \kappa \boldsymbol{\nu} \delta(\boldsymbol{x} - \boldsymbol{x}_s) \;,
\end{aligned}
$$

where ρ and μ are the local values of density and dynamic viscosity, respectively. In equation (1) p is the pressure, $\boldsymbol{f}$ denotes the mass forces, σ is the surface tension coefficient, κ is the local curvature of the interface and $\boldsymbol{\nu}$ is the unit normal vector at the interface oriented toward the air. In equation (1) the term $\delta(\boldsymbol{x}-\boldsymbol{x}_s)$ represents the Dirac function which is zero out of the interface location $\boldsymbol{x}_s$.

The Navier-Stokes equations are written in generalized variables and discretized onto a non staggered grid. The system is solved through a fractional step approach: the momentum equation is advanced in time by neglecting pressure terms (*Predictor step*) whose effects are successively reintroduced by enforcing the continuity of the velocity field (*Corrector step*). The diagonal part of the dominating diffusive terms is accounted implicitly with a Crank-Nicolson scheme, whereas the other viscous terms, related to the non uniformity of the viscosity and to the grid distortion, are computed explicitly. A low-storage, three-steps Runge-Kutta is adopted for the explicit terms. The Poisson equation for the pressure corrector term is solved with a Biconjugate gradient stabilized (BiCGstab) algorithm (van der Vorst, 1992).

The interface is captured through a Level-Set algorithm. The signed distance d from the interface is reinitialized at each step and is convected with the transport equation:

$$
\frac{\partial d}{\partial t} = -\boldsymbol{u} \cdot \nabla \boldsymbol{u} \;,
$$

which ensure that all particles belonging to the free surface ($d = 0$) continue to stay there, as the kinematic boundary condition requires. The surface tension contribution to the momentum equation is approximated by a continuum model as suggested in Brackbill et al. (1992). A more extensive discussion of the numerical model and its validation and verification is given in Iafrati and Campana (2005).

3. INITIAL FREE–SURFACE PROFILE

A periodic wave profile is initialized as

$$\eta(x,0) = \frac{a}{\lambda}\left(\cos(kx) + \frac{1}{2}\varepsilon\cos(2kx) + \frac{3}{8}\varepsilon^2\cos(3kx)\right) \ ,$$

(2)

where $k = 2\pi/\lambda$ is the fundamental wavenumber, $\varepsilon = ak$ is the initial wave steepness and λ is the fundamental wavelength. The fundamental wavelength is taken as reference value for lengths, whereas $U_r = \sqrt{\lambda g}$ is assumed as reference value for the velocities. The initial velocity field in water is assigned as

$$u = \Omega a \exp(ky)\cos(kx) \ , \qquad v = \Omega a \exp(ky)\sin(kx) \ ,$$

(3)

where $\Omega = \sqrt{gk(1+\varepsilon^2)}$ accounts for the nonlinear correction (Whitham, 1974).

Note that equation (2) is not exactly a third order Stokes wave as the secular term is missing (Grue *et al.*, 2003). The purpose of the present paper is to generate breaking of different intensities and to see to which extent the different breaking intensity affects the air entrainment process. In this regard the lack of the secular term has only a minor effect on the results, as it is discussed in Iafrati (2008).

At the beginning of the simulation the flow in air is assumed to be at rest, and the motion occurring in air in the later stage is induced by the momentum exchange at the interface operated by both tangential and normal stresses. No-slip boundary conditions are assigned at the top and bottom boundaries. As the water depth is of the order of half of the fundamental wavelength, this choice does not affect remarkably the dynamics of the breaking process (Chen *et al.*, 1999). Also, for such wavelength-depth ratio, the energy loss by bottom friction is essentially negligible (Lighthill, 1978). In all cases it is assumed

$$We = g^{1/2}\lambda\sqrt{\frac{\rho_w}{\sigma}} = 100 \ ,$$

which corresponds to water waves of about 30 centimeters wavelength. For such wavelength the Reynolds number is

$$Re = \frac{\rho_w g^{1/2}\lambda^{3/2}}{\mu_w} \simeq 4.4 \times 10^5 \ ,$$

which is too high, even for a two-dimensional solver, for all the scales to be accurately resolved. For this reason numerical simulations are carried out at $Re = 10^4$, whereas a more careful discussion of the role played by the Reynolds number on the solution is provided in Iafrati (2008). The density ratio is assumed to be equal to the real one for air and water, which is $\rho_a/\rho_w = 0.00125$, whereas the viscosity ratio is $\mu_a/\mu_w = 0.04$, the same used by Chen *et al.*, (1999).

The computational domain is one fundamental wavelength wide and one fundamental wavelength high, that is $x,y \in [-0.5, 0.5]$, and it is discretized by 512×512 grid cells, uniformly spaced. For the case with $\varepsilon = 0.65$, large drops with high upward velocity components are generated by the plunging of the jet and a higher computational domain, with $y \in [-0.5, 1.5]$ and a 512×1024 grid, is used. In the numerical simulations it is assumed $\delta_P = \delta_T = 0.005$

which means that density and viscosity jumps and surface tension forces are spread across a region which is about five grid cells thick. As lengths are scaled by the wavelength, for a 30 centimeters wave the cell size is about 0.6 millimiters and the thickness of the transition region corresponds to 3 millimiters. This physical value is important in order to relate the present numerical results with the experimental findings by Deane and Stokes (2002).

In order to investigate to which extent the initial wave steepness changes the phenomena involved in the breaking event, numerical simulations are carried out by varying ε in the range 0.2 to 0.65. It is found that the breaking is of the spilling type for $\varepsilon = 0.33$ and $\varepsilon = 0.35$ whereas it is of the plunging type for $\varepsilon > 0.37$.
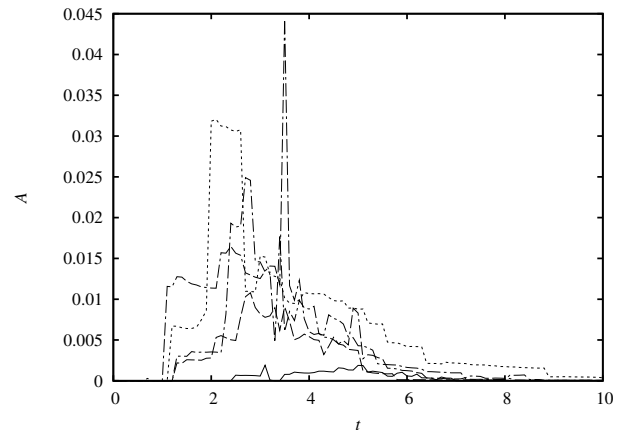

Figure 1: Time histories of the total area of the air bubbles entrained by the breaking process. Results refer to $\varepsilon = 0.40$ (*solid*), $\varepsilon = 0.50$ (*dash*), $\varepsilon = 0.55$ (*dash-dot*), $\varepsilon = 0.60$ (*dot*), $\varepsilon = 0.65$ (*dash-dash-dot*).

4. AIR ENTRAINMENT AND DEGASSING PHASE

The detailed information provided by the numerical solution allows a quantitative investigation of the air entrainment and of the degassing process. In Fig. 1 the time histories of the total area of air entrained by the plunging breaking event at different steepnesses are drawn. The curves show the entrapment of the large air cavity at the breaking onset. After a time interval during which the area remains constant, the time histories evidence a sharp rise and a subsequent drop which are related to the plunging of the splash up jet. As the filament of water that encompasses the cavity is rather thin, it quickly collapses, letting the air in the cavity to escape, as it can be seen by comparing the time history of the entrapped air for $\varepsilon = 0.6$, drawn in Fig. 2, with the free–surface profiles at $t = 2.0$ and $t = 2.7$ given in Fig. 3.

Figure 1 indicates that, in a later stage, the amount of air entrapped decays with time. From the free–surface profiles given in Fig. 4 it can be seen that bubbles gradually rise back towards the free–surface and eventually escape from the water. Although the above mechanism is the main responsible for the degassing of the air bubbles, before drawing any quantitative estimate of the degassing process it is important to analyze the limits imposed by the adopted grid discretization in connection with the smallest bubbles.
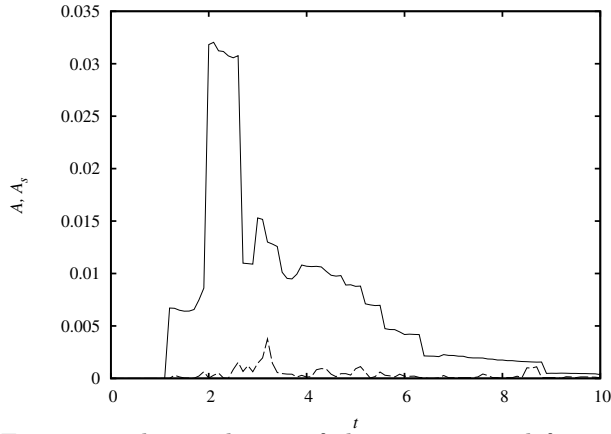
Figure 2: The total area of the air entrained for $\varepsilon = 0.60$ (*solid*) is drawn along with the corresponding area of the unresolved bubbles.

As the free surface is captured on the basis of the change in the sign of the distance function at two successive nodes of the grid, the model cannot describe a closed contours thickness of which is smaller than one grid cell, i.e. 0.6 millimiters. Furthermore, due to the spreading of the density and viscosity jumps across a transition layer of thickness $2\delta_P$, bubbles or air filaments thinner than $2\delta_P$, which is about 3 millimeters, cannot be considered fully resolved. So, in order to estimate which portion of the entrained bubbles is resolved, an average thickness is evaluated as the ratio between the area of the bubble and the maximum between the horizontal and vertical dimensions of the bubble. A bubble is considered unresolved when the average thickness fails below $2\delta_P$.
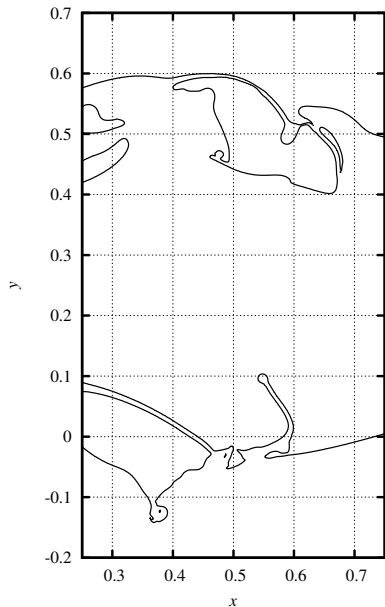

Figure 3: The free–surface profiles at $t = 2.0$ and $t = 2.7$ for $\varepsilon = 0.60$ are compared to show the entrapment and the subsequent release of a large air bubble by the splash up jet. A vertical shift of 0.5 is applied between the two profiles to make the comparison easier.

In Fig. 2 the total area of the unresolved bubbles A_s is drawn together with the total area of the entrapped air A for the case $\varepsilon = 0.60$. The figure indicates that the area of the unresolved bubbles is very small compared to the total

area up to about half wave period after the breaking onset. Next, due to the fragmentation of the air cavity it grows and it gets up to one fourth of the total area.
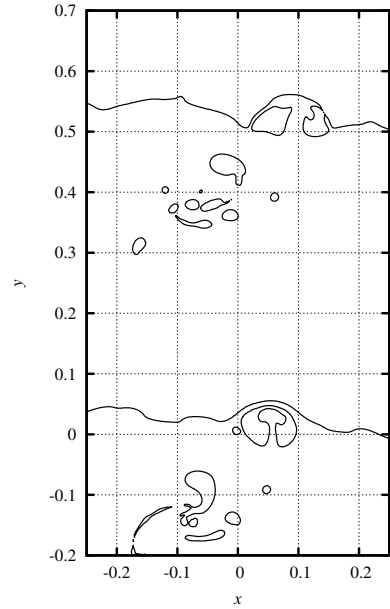

Figure 4: The free–surface profiles for $\varepsilon = 0.60$ at $t = 5.0$ and $t = 5.2$ are compared to show the vertical rise of the air bubbles towards the free–surface. Also in this case a vertical shift is applied.
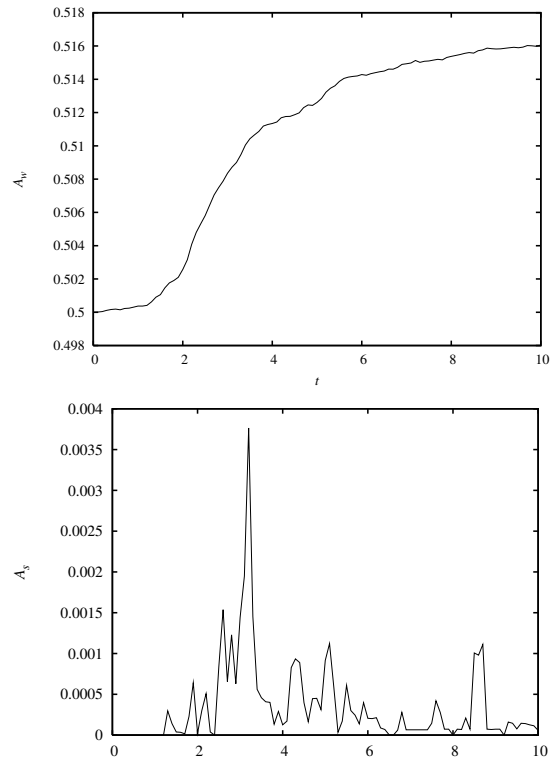

Figure 5: Time histories of the total area occupied by water A_w (*top*) and of the unresolved bubbles A_s (*bottom*) for the case $\varepsilon = 0.60$.

The artificial degassing of thin air filaments or bubbles operated by the numerical scheme, can be quantitatively estimated from the total area occupied by water A_w, drawn in the top of Fig. 5 for the case $\varepsilon = 0.60$. The comparison

with the corresponding area of the unresolved bubbles given on the bottom of Fig. 5, indicates that the sharpest increase in the water area occurs between $t = 2.0$ and $t = 4.0$, during which the total area of the unresolved bubbles take the largest values. In total, at the end of the numerical simulation, the artificial degassing can be estimated in about three per cent of initial water area.

With the aim of deriving a quantitative estimate of the degassing rate, the time histories of the total area occupied by air bubbles are scaled by the area A_0 of the air cavity entrapped at the breaking onset. Results, drawn in Fig. 6, are compared with the decay rate proposed by Lamarre and Melville (1991), who found that the scaled air volume behaves as $C \exp(-3.9(t-t_b)/T)$, where t_b is the time of breaking onset and T is the wave period. In Lamarre and Melville (1991) the constant $C = 2.6$ accounts for the initial period, duration of which is approximately $T/4$, during which the amount of air entrapped remains nearly constant.
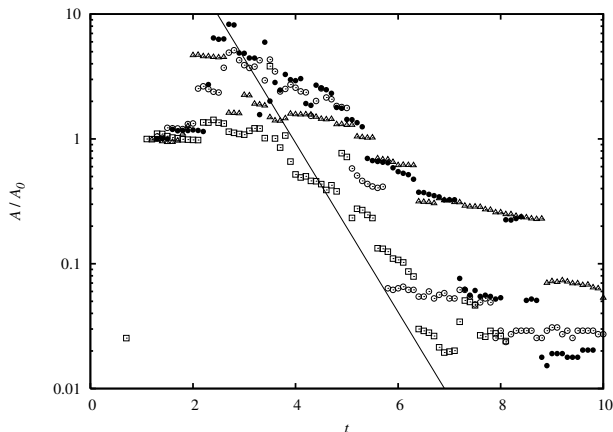

Figure 6: Time histories of the total area of the entrapped bubbles divided by the area of the air cavity generated at the breaking onset A_0. Results refer to $\varepsilon = 0.50$ ($\circ$), $\varepsilon = 0.55$ ($\bullet$), $\varepsilon = 0.60$ ($\triangle$), $\varepsilon = 0.65$ ($\square$). The line represent the exponential decay rate $C \exp(-3.9(t - t_b)/T)$ where $t_b = 1$, $T = 2.5$ and $C = 10^2$.

In the comparison established below it is assumed $t_b = 1$ and $T = 2.5$ whereas a different value of the constant $C = 10^2$ is needed to get a better agreement. In Iafrati (2008) it is explained that the different constant is needed to because, due to a standing wave component generated by the initial free surface profile, a second breaking event takes place. The occurrence of the second plunging event and to the new splash up, keeps the amount of entrapped air constant for a longer period. Aside from the different constant, the comparison shown in Fig. 6 indicates that the curves follow the exponential decay in the early stage. In a later stage, probably because of the difficulties of the numerical model in achieving a complete description of the fragmentation process, numerical results display a lower decay rate.

In order to achieve a quantitative estimate of the effects of the breaking intensity on the amount of air entrapped, in Fig. 7 the area of the air cavity entrapped at the onset of the stronger breaking cases are drawn versus the steepness. The data indicate that, for the range of steepnesses considered here, the area of the air cavity entrapped by the

first breaking event grows as ε^7. At present it is not possible to estimate to which extent such relation depends on the initial conditions adopted here. A deeper investigation is planned for the future in which a similar analysis will be carried out by using different methods to induce breaking.
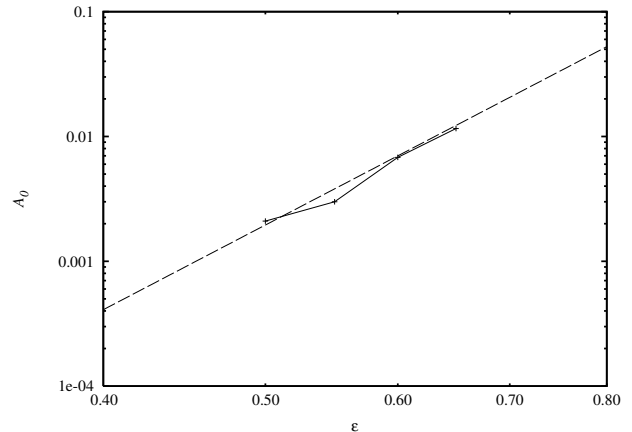

Figure 7: Area of the air cavity entrapped at the breaking onset versus the steepness.

6. ACKNOWLEDGMENTS

7. REFERENCES

M. Brocchini and D.H. Peregrine (2001) *The dynamics of strong turbulence at free surfaces. Part 1. Description*, J. Fluid Mech., 449, 225–254.

E. Lamarre and W.K. Melville (1991) *Air entrainment and dissipation in breaking waves*, Nature, 351, 469–472.

C.E. Blenkinsopp and J.R. Chaplin (2007) *Void fraction measurements in breaking waves*, Proc. R. Soc. Lon., A 463, 3151–3170.

G.B. Deane and M.D. Stokes (2002) *Scale dependence of bubble creation mechanisms in breaking waves*, Nature, 418, 839–844.

H.A. van der Vorst (1992) *Bi-CGSTAB: fast and smoothly converging variant of Bi-CG for the solution of nonsymmetric linear systems*, SIAM J. Sci. Stat. Comput., 13, 631–644.

J.U. Brackbill, D.B. Kothe and C. Zemach, (1992) *A continuum method for modeling surface tension*, J. Comput. Phys., 100, 335–354.

A. Iafrati and E.F. Campana, (2005) *Free surface fluctuations behind microbreakers: space–time behaviour and subsurface flow field*, J. Fluid Mech., 529, 311–347.

G.B. Whitham, (1974) Linear and nonlinear waves, Wiley Interscience

J. Grue, D. Clamond, M. Huseby and A. Jensen, (2003) *Kinematics of extreme water waves*, 25, 355–366.

A. Iafrati (2008)

G. Chen, C. Kharif, S. Zaleski and J. Li (1999) *Two-dimensional Navier–Stokes simulation of breaking waves*, Phys. Fluids, 11, 121–133.

J. Lighthill (1978) Waves in Fluids, Cambridge Univ.